

ARTICLE

Open Access

# Dual-responsive disassembly of core-shell nanoparticles with self-supplied H<sub>2</sub>O<sub>2</sub> and autocatalytic Fenton reaction for enhanced chemodynamic therapy

Mengran Peng<sup>1</sup>, Enguo Ju<sup>1</sup>, Yanteng Xu<sup>1</sup>, Yuqin Wang<sup>1</sup>, Shixian Lv<sup>2</sup>, Dan Shao<sup>3</sup>, Haixia Wang<sup>1</sup>, Yu Tao<sup>1</sup>, Yue Zheng<sup>1</sup> and Mingqiang Li<sup>1,4</sup>

## Abstract

Chemodynamic therapy holds great potential for cancer treatment due to its reliable curative effects, minimal invasiveness, and few systemic side effects. However, the limited amount of intracellular H<sub>2</sub>O<sub>2</sub> makes achieving high-performance chemodynamic therapy challenging. Herein, we report a core-shell nanoplatform with dual-responsive disassembly that self-supplies H<sub>2</sub>O<sub>2</sub> and undergoes an autocatalytic Fenton reaction for enhanced chemodynamic therapy. The platform was designed by coating glucose oxidase-mimicking nanozyme gold nanoparticles (AuNPs) with a metal-polyphenol network (Au@MPN). Both ATP and low pH can disassemble the Au@MPN to release Fe(III), which can then be reduced into Fe(II) by the simultaneously released tannic acid (TA). In particular, the exposed AuNPs can catalyze the oxidation of intracellular glucose to produce H<sub>2</sub>O<sub>2</sub>. Subsequently, Fe(II) and the self-supplied H<sub>2</sub>O<sub>2</sub> induce an efficient Fenton reaction for chemodynamic therapy by generating hydroxyl radicals ( $\cdot$ OH) that are highly toxic to cancer cells. Moreover, tumor growth can be effectively suppressed after both intratumoral and intravenous Au@MPN administration. Additionally, metastatic melanoma lung tumors could be inhibited by intratracheal instillation of Au@MPN. Thus, this work not only reports a facile method to construct a chemodynamic agent with self-supplied H<sub>2</sub>O<sub>2</sub> and high therapeutic efficiency but also provides insight into the design of nanoplatforms with enhanced efficiency for chemodynamic therapy.

## Introduction

Malignant melanoma is one of the fastest growing skin cancers with a high degree of malignancy, early metastasis, high mortality, and extremely poor prognosis, and its clinical treatment poses great challenges<sup>1</sup>. Surgical

treatment is the main method for melanoma therapy. Early melanoma can be cured through expanded resection of the lesion, but there are risks of postoperative tumor residue, recurrence, metastasis, and surgical complications<sup>2</sup>. Radiotherapy also has a limited effect on treating malignant melanoma, as its effect is highly dependent on oxygen status and the growth cycle of the tumor, and it comes along with many side effects<sup>3</sup>. Chemotherapeutic drugs such as dacarbazine and temozolomide can effectively kill tumor cells, but their drawbacks mainly include dose-dependent toxicity, side effects, and easy destruction of the immune functions of the patient, which in turn will accelerate the spread of residual cancer cells in the body<sup>4</sup>. Targeted therapy including BRAF inhibitors and MEK

Correspondence: Enguo Ju ([jueng@mail.sysu.edu.cn](mailto:jueng@mail.sysu.edu.cn)) or Yu Tao ([taoy28@mail.sysu.edu.cn](mailto:taoy28@mail.sysu.edu.cn)) or Yue Zheng ([zhengy58@mail.sysu.edu.cn](mailto:zhengy58@mail.sysu.edu.cn)) or Mingqiang Li ([limq567@mail.sysu.edu.cn](mailto:limq567@mail.sysu.edu.cn))

<sup>1</sup>Laboratory of Biomaterials and Translational Medicine, Center for Nanomedicine, Department of Dermato-Venereology, The Third Affiliated Hospital, Sun Yat-sen University, 510630 Guangzhou, China

<sup>2</sup>School of Materials Science and Engineering, Peking University, 100871 Beijing, China

Full list of author information is available at the end of the article  
These authors contributed equally: Mengran Peng, Enguo Ju, Yanteng Xu

© The Author(s) 2022

 **Open Access** This article is licensed under a Creative Commons Attribution 4.0 International License, which permits use, sharing, adaptation, distribution and reproduction in any medium or format, as long as you give appropriate credit to the original author(s) and the source, provide a link to the Creative Commons license, and indicate if changes were made. The images or other third party material in this article are included in the article's Creative Commons license, unless indicated otherwise in a credit line to the material. If material is not included in the article's Creative Commons license and your intended use is not permitted by statutory regulation or exceeds the permitted use, you will need to obtain permission directly from the copyright holder. To view a copy of this license, visit <http://creativecommons.org/licenses/by/4.0/>.

inhibitors is suitable only for tumor patients with corresponding mutations<sup>5</sup>. As one of the most popular areas of cancer research in recent years, immunotherapy, especially with immune checkpoint inhibitors, presents a good therapeutic effect against malignant melanoma<sup>6–8</sup>. However, side effects, including immune pneumonia and immune myocarditis, limit its broad application<sup>9</sup>.

Recently, chemodynamic therapy has sparked great interest owing to its high efficiency and anticancer mechanism that is distinct from traditional cancer treatment<sup>10,11</sup>. Taking advantage of nanotechnologies and nanomaterials, researchers have rationally designed catalysts that once combined with the unique microenvironment of tumors can improve the Fenton/Fenton-like reaction<sup>12–14</sup>. As an essential reactant for Fenton/Fenton-like reactions, a high concentration of  $\text{H}_2\text{O}_2$  is desired for generating sufficient hydroxyl radicals ( $\cdot\text{OH}$ ). However, the limited amount of intracellular  $\text{H}_2\text{O}_2$  greatly restricts the application of chemodynamic therapy. To solve this problem, a self-supplied  $\text{H}_2\text{O}_2$  strategy was proposed for the in situ generation of  $\text{H}_2\text{O}_2$  inside cancer cells<sup>15,16</sup>. Various materials have been applied for this purpose, such as  $\text{CaO}_2$ <sup>17,18</sup>,  $\text{CuO}_2$ <sup>19</sup>, and glucose oxidase<sup>20</sup>. Among them, glucose oxidase, which can catalyze the oxidation of glucose to generate  $\text{H}_2\text{O}_2$ , holds great potential for boosting the  $\text{H}_2\text{O}_2$  supply. However, as a natural protein, glucose oxidase suffers from poor stability, a short half-life

in vivo, and immunogenicity<sup>21</sup>. As an alternative, nanozymes that mimic glucose oxidase have various advantages over natural enzymes, such as low expense, ease of manufacturing, and maintenance of activity over broad ranges of pH and temperature<sup>22,23</sup>. For example, Zhang et al. reported the immobilization of ultrasmall gold nanoparticles (AuNPs) on hollow mesoporous organosilica nanoparticles with Cu(II)-tannic complexes deposited on the surface to self-supply  $\text{H}_2\text{O}_2$  for chemodynamic therapy<sup>24</sup>. In addition, Ding et al. demonstrated a metal-organic framework as a platform for the in situ growth of small AuNPs on the surface to oxidize intracellular glucose to produce  $\text{H}_2\text{O}_2$ <sup>25</sup>. Although promising, the complexity of the synthetic process makes controllable, reproducible and large-scale production challenging<sup>26</sup>. Therefore, it is highly desired to fabricate robust and facile nanoplatforms that can self-supply  $\text{H}_2\text{O}_2$  with high performance for chemodynamic therapy.

Herein, we report the dual-responsive disassembly of a core-shell nanoplatform with self-supplied  $\text{H}_2\text{O}_2$  and the ability to carry out an autocatalytic Fenton reaction for enhanced chemodynamic therapy (Fig. 1). The platform was constructed by coating the surface of glucose oxidase-mimicking nanozyme with a metal-polyphenol network (Au@MPN), which could be disassembled by either ATP or an acidic environment. In addition, the Fe(III) released from Au@MPN could be reduced by the released tannic

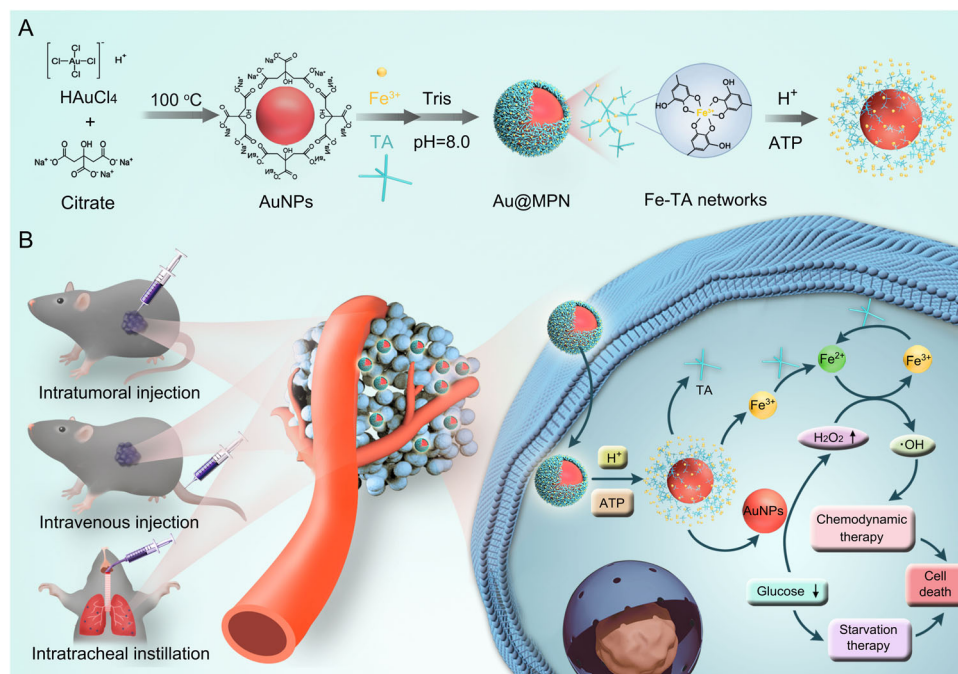


**Fig. 1** Schematic illustration of the Au@MPN with the ability to self-supply  $\text{H}_2\text{O}_2$  for enhanced chemodynamic therapy. **A** Preparation of Au@MPN and their disassembly process in the presence of ATP or in an acidic environment. **B** The antitumor mechanism of Au@MPN for enhanced chemodynamic therapy.

acid (TA) into Fe(II), which exhibited higher catalytic performance than Fe(III). In particular, the exposed AuNPs catalyzed glucose oxidation to produce sufficient  $\text{H}_2\text{O}_2$  in situ, which subsequently reacted with Fe(II) to trigger the Fenton reaction and generate highly toxic hydroxyl radicals ( $\bullet\text{OH}$ ). Moreover, the in vivo antitumor efficacy of Au@MPN was demonstrated after both intratumoral and intravenous administration. Additionally, metastatic melanoma lung tumors could be inhibited by intratracheal instillation of Au@MPN. Therefore, this work may provide insight into the design of nanoplat-forms with enhanced efficiency for tumor therapy.

## Materials and methods

### Materials

Ferric chloride hexahydrate ( $\text{FeCl}_3 \cdot 6\text{H}_2\text{O}$ ), tannic acid (TA), chloroauric acid trihydrate ( $\text{HAuCl}_4 \cdot 3\text{H}_2\text{O}$ ), methylene blue (MB), 1,10-phenanthroline monohydrate, and glucose were purchased from Aladdin-Reagent Co. Ltd. 2',7'-Dichlorofluorescein diacetate (DCFH-DA) was obtained from Beyotime. 3,3',5,5'-Tetramethylbenzidine (TMB) was purchased from Sigma-Aldrich. The horseradish peroxidase (HRP) enzyme was purchased from Macklin. An annexin V-FITC/PI apoptosis detection kit was provided by KeyGen Biotech. Co., Ltd. All other materials were commercially available and used as received unless otherwise noted.

### Instrumentation

Transmission electron microscopy (TEM) images were captured by an FEI Tecnai G20 S-TWIN microscope operating at an accelerating voltage of 120 kV. The elemental binding energy of Au@MPN was measured by X-ray photoelectron spectroscopy (ESCALab 250, Thermo Fisher). The hydrodynamic size and zeta potential were evaluated by a particle analyzer (Litesizer 500, Anton Paar). The UV – vis absorbance was measured by a UV – vis spectrophotometer (UV 2600, Shimadzu).

### Synthesis of AuNPs

AuNPs were synthesized according to a previously reported method<sup>27</sup>. Vials and stirrers were washed with aqua regia before use. First, 0.4 mL of  $\text{HAuCl}_4$  (24.3 mM) was added to 9.6 mL of Milli-Q water ( $\text{ddH}_2\text{O}$ ). The solution was heated with continuous magnetic stirring. When it was violently boiling, 1 mL of trisodium citrate (38.8 mM) was added and the mixture was stirred for another 30 min. After cooling to room temperature, the prepared AuNPs were stored at 4 °C for further use.

### Synthesis of Au@MPN and Au@MPN/PEG

AuNPs (0.8 mL, 24.3 mM) were placed into a 1.5 mL centrifuge tube. Two microliters of TA (40.8 mg/mL) was mixed with the AuNPs and vortexed for 20 s. Then, 2  $\mu\text{L}$  of

$\text{FeCl}_3$  (24 mM) was added before vortexing for 20 s. Next, 200  $\mu\text{L}$  of Tris buffer (50 mM, pH 8.0) was added, and the mixture was vortexed for 20 s. The solution was then centrifuged at  $1 \times 10^4 g$  for 10 min and washed with  $\text{ddH}_2\text{O}$  twice to obtain Au@MPN. The concentrations of Au and Fe in the prepared Au@MPN were determined by ICP to be 25.3 and 3.1  $\mu\text{g}/\text{mL}$ , respectively. Au@MPN with different Au/Fe ratios were synthesized using the same procedure, except that the concentration of  $\text{FeCl}_3$  was changed.

Au@MPN/PEG were prepared as follows. First, Au@MPN (2 mg/mL) were redispersed in 1 mL of phosphate-buffered saline (PBS, pH 7.4) in a 1.5 mL Eppendorf tube. Then, 1 mg of PEG-NH<sub>2</sub> was added to the above tube, which was kept at room temperature under magnetic stirring for 2 h. Excess PEG-NH<sub>2</sub> was removed by centrifugation for 10 min at 13,000 rpm to obtain Au@MPN/PEG.

### Release of Fe(III) from Au@MPN

Au@MPN (25 mg/mL) were placed in a dialysis bag (MWCO: 14 kDa), which was then immersed in 10 mL of different solutions containing varying concentrations of ATP (0.5 mg/mL, 1 mg/mL, and 2 mg/mL) or buffers with different pH values (pH 4.0 and pH 5.0). Each dialysis bag was placed on a horizontal shaker (100 rpm) under stirring. Then, 1 mL of buffer was withdrawn, and fresh buffer was added at the indicated time points. The withdrawn buffer was mixed with hydroxylamine hydrochloride for 15 min, followed by the addition of 1,10-phenanthroline. Finally, the absorption at 510 nm was measured to calculate the concentration of released Fe(III) according to the standard curve.

### Measurement of Fe(II) content

The content of Fe(II) in various samples was determined by a method similar to that described above except that hydroxylamine hydrochloride was not needed. Briefly, samples taken at different times were dissolved in PBS containing ATP (1 mg/mL) and 1,10-phenanthroline. Then, the absorbance at 510 nm was measured to calculate the concentration of Fe(II) according to the standard curve.

### Measurement of glucose oxidase-like activity

The quantitative determination of  $\text{H}_2\text{O}_2$  production was carried out by using the classic colorimetric method. First, 50  $\mu\text{L}$  of AuNPs (24 mM) were mixed with 100  $\mu\text{L}$  of 200 mM glucose solution for different lengths of time (hours) and named solution A. A total of 289  $\mu\text{L}$  of acetate buffer (0.1 M, pH 4.0), 6  $\mu\text{L}$  of TMB (10 mg/mL) and 5  $\mu\text{L}$  of HRP (1 mg/mL) were mixed to generate solution B. Then, 100  $\mu\text{L}$  of solution A was added to solution B for 10 min of reaction. Finally, the absorbance at 650 nm was measured and recorded. This same method was applied to detect  $\text{H}_2\text{O}_2$  produced by the reaction of AuNPs and different concentrations of glucose.

### Evaluation of the generation of •OH

The production of •OH was detected by a UV–Vis spectrophotometer with MB serving as a sensor. In brief, 500  $\mu\text{L}$  of glucose (1 M), 50  $\mu\text{L}$  of MB (0.25 mM) and 100  $\mu\text{L}$  of Au@MPN (7 mg/mL, 14 mg/mL, and 35 mg/mL) were mixed with a solution containing 500  $\mu\text{L}$  of ATP (2 mg/mL). Then, different volumes of ddH<sub>2</sub>O were added to the solution to reach a final volume of 1500  $\mu\text{L}$ . After 4 h, the UV–Vis absorption of MB solution was measured. This same method was applied to detect •OH under different conditions (without H<sub>2</sub>O<sub>2</sub> and glucose, without H<sub>2</sub>O<sub>2</sub>, without glucose, and with H<sub>2</sub>O<sub>2</sub> and glucose).

### Cell culture

B16F10 cells (obtained from the Cell Bank of Shanghai Institute of Biochemistry and Cell Biology, Chinese Academy of Sciences) were cultured in DMEM supplemented with 10% fetal bovine serum (FBS), streptomycin (100  $\mu\text{g}/\text{mL}$ ) and penicillin (100 unit/mL) at 37 °C in a humidified atmosphere with 5% CO<sub>2</sub>.

### Cellular uptake of Au@MPN

Rhodamine B-loaded Au@MPN were used to investigate cellular uptake. Rhodamine B-loaded Au@MPN were prepared as follows. First, 0.8 mL of AuNPs (24.3 mM) was mixed with 100  $\mu\text{L}$  of rhodamine B (2 mg/mL) in a 1.5 mL centrifugal tube. Then, 2  $\mu\text{L}$  of TA (40.8 mg/mL) was added and the mixture was vortexed for 20 s. Next, 2  $\mu\text{L}$  of FeCl<sub>3</sub> (24 mM) was added for 20 s of vortexing. Finally, 200  $\mu\text{L}$  of Tris buffer (50 mM, pH 8.0) was added before vortexing for 20 s. The rhodamine B-loaded Au@MPN were obtained by centrifugation (13,000 rpm for 10 min) and repeated washings with ddH<sub>2</sub>O until fluorescence could no longer be detected in the supernatant.

To study the cellular uptake of Au@MPN, B16F10 cells were seeded in a 24-well plate overnight for attachment and then incubated with rhodamine B-loaded Au@MPN for the indicated lengths of time. After washing the cells with PBS twice, the nuclei of the cells were stained with Hoechst 33342. The cells were subsequently examined by fluorescence microscopy (Zeiss Axio Observer 3) or flow cytometry (Beckman, CytoFLEX).

### In vitro cytotoxicity assay

The cytotoxicity of Au@MPN was evaluated using the MTT assay. Briefly, B16F10 cells were seeded into 96-well plates overnight. Then, the cells were treated with Au@MPN and incubated for another 24 h. Subsequently, MTT reagent was added. Four hours later, the formazan crystals were dissolved with dimethyl sulfoxide. Finally, the absorbance at 570 nm was measured and recorded using a microplate reader (Synergy H1, BioTek).

### Detection of intracellular reactive oxygen species (ROS)

B16F10 cells were seeded in 12-well plates overnight. Then, the cells were incubated with PBS, ROSup, Au@MPN (7 mg/mL), or Au@MPN (14 mg/mL), followed by staining with DCFH-DA (10  $\mu\text{M}$ ) for 30 min. Finally, the cells were observed by fluorescence microscopy or analyzed via flow cytometry.

### Live/dead staining assay

B16F10 cells were seeded in 12-well plates overnight. Then, the cells were incubated with PBS, AuNPs (7 mg/mL), or Au@MPN (7 mg/mL) for 8 h. After that, the cells were stained with calcein-AM and PI and observed by fluorescence microscopy.

### Cell apoptosis assessment

B16F10 cells were seeded in 12-well plates overnight. Then, the cells were incubated with PBS, AuNPs (7 mg/mL), or Au@MPN (7 mg/mL) for 24 h. Next, the cells were stained with annexin V-FITC and PI for 15 min according to the manufacturer's protocol. Finally, the cells were collected and analyzed by flow cytometry.

### In vivo antitumor effect of Au@MPN

All live animal experiments were conducted according to the protocols of the Institutional Animal Care and Use Committee of the Animal Experiment Center of Sun Yat-sen University. Female C57 mice at 6 weeks of age were subcutaneously injected with B16F10 cells (10<sup>6</sup> cells in 0.1 mL). When the tumors reached a volume of 50 mm<sup>3</sup>, the mice were injected with 0.1 mL of PBS, 0.1 mL of AuNPs (7 mg/mL), or 0.1 mL of Au@MPN (7 mg/mL) either intratumorally or intravenously. The lengths and widths of the tumors were measured every 2 days. Tumor volume was calculated as follows: tumor volume (V) = (tumor length)  $\times$  (tumor width)<sup>2</sup>/2. Tumors from each group were collected and photographed. Additionally, the major organs were collected, fixed in a 4% paraformaldehyde solution, and stained with hematoxylin and eosin (H&E) for histological analysis.

Metastatic lung tumors were established by injecting B16F10 cells into mice through the tail vein. Then, a handheld aerosolizer (Liquid Aerosol Devices, Micro-Sprayer Aerosolizers) was employed to inject PBS, AuNPs, or Au@MPN by intratracheal instillation. On Day 12, the mice were sacrificed, and images of the lungs were captured. The lungs were also stained with H&E and examined under a microscope.

### Statistical analysis

Data are presented as the mean  $\pm$  standard deviation. Statistical analyses were performed using GraphPad Prism 7.0. One-way ANOVA was conducted for the analysis of significant differences, and Tukey's test was used for post

hoc analysis. Statistical significance was defined as  $*p < 0.05$ ,  $**p < 0.01$ , and  $***p < 0.005$ .

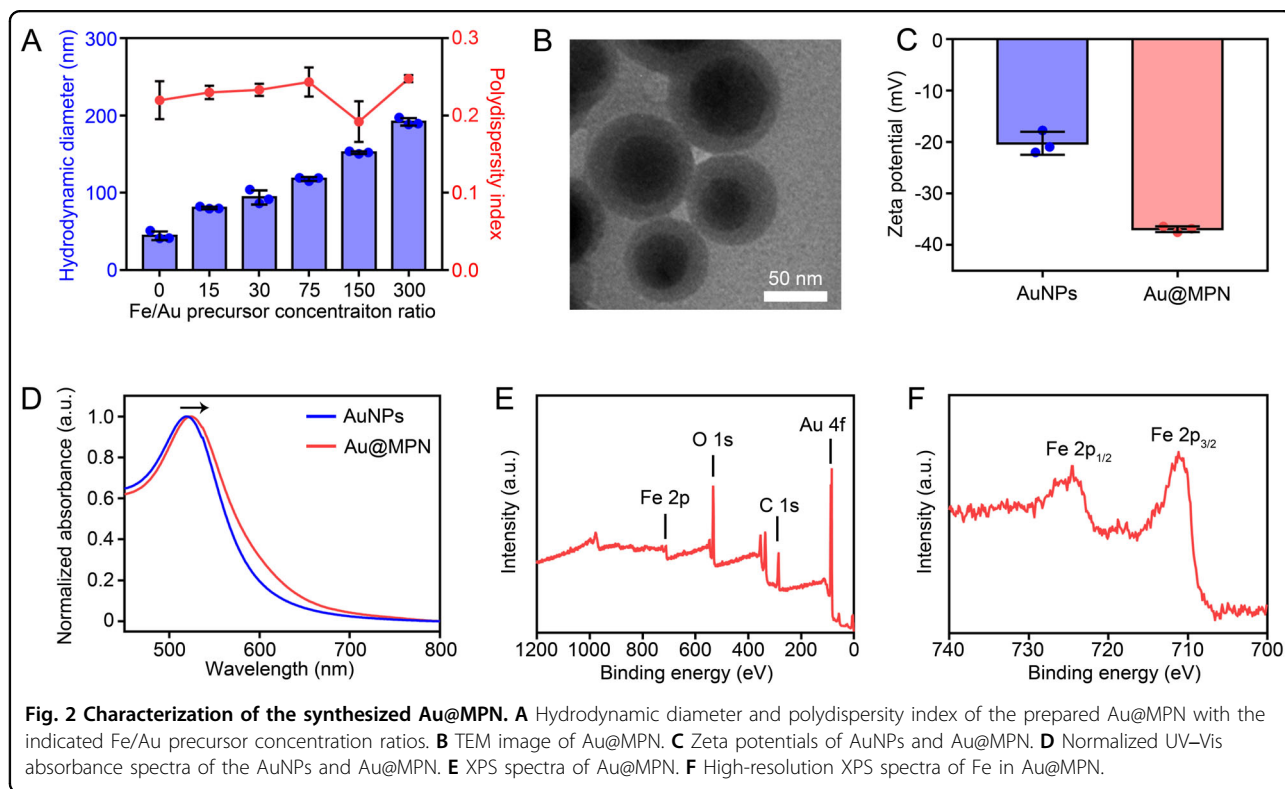
## Results and discussion

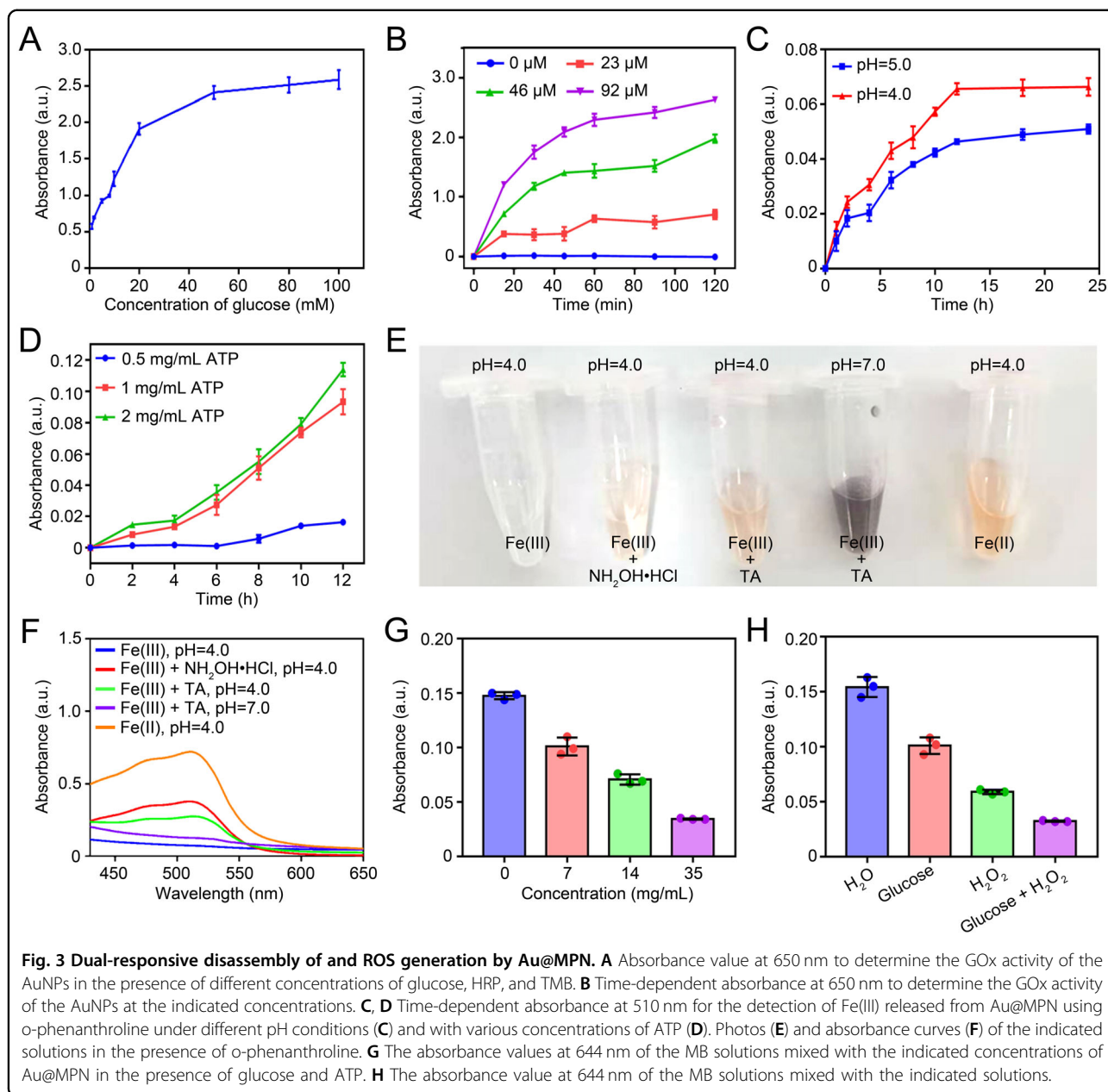
### Synthesis and characterization of Au@MPN

The procedure for the synthesis of Au@MPN is depicted in Fig. 1. First, AuNPs were prepared using trisodium citrate as the stabilizing agent as well as the reducing agent, followed by the addition of  $\text{FeCl}_3$  and TA to form the layer of MPN on the surface of AuNPs. Using a two-step synthetic strategy employing presynthesized AuNPs as building blocks offers better controllability of the structure and morphology by rationally tuning the ratio of precursors<sup>28</sup>. As expected, the thickness of the MPN layer could be adjusted by altering the Fe/Au precursor concentration ratio (Fig. 2A). TEM images of Au@MPN clearly showed a spherical morphology and core-shell structure with a diameter of  $\sim 50$  nm (Fig. 2B). The successful adsorption of the formed MPN on the AuNP surface may be ascribed to the universal adhesive property of polyphenols<sup>29</sup>. Moreover, the  $\zeta$ -potential revealed that both the AuNPs and Au@MPN were negatively charged (Fig. 2C). The UV-Vis absorption peak of Au@MPN showed a redshift of several nanometers compared to that of AuNPs with a typical peak at 520 nm, which was attributed to the fact that the refractive index of the shell is higher than that of water (Fig. 2D)<sup>30</sup>. Additionally, X-ray photoelectron spectroscopy (XPS) confirmed the

presence of Au, Fe, C, and O in the Au@MPN (Fig. 2E). In addition, there were two prominent peaks at 87.58 and 83.93 eV, which were assigned to the Au  $4f_{7/2}$  and Au  $4f_{5/2}$  signals of metallic Au (Fig. S1). Of note, the Fe 2p signal revealed peaks at 711.18 and 724.48 eV, which are consistent with the typical signals of Fe(III) species<sup>31</sup>. The above results confirmed the existence of coordination bonds between Fe(III) and the phenolic groups of TA.

To examine the glucose oxidase-like activity of the synthesized AuNPs, the produced  $\text{H}_2\text{O}_2$  was detected in a reaction system containing AuNPs and glucose using the HRP-catalyzed oxidation of TMB, and the absorbance at 650 nm was measured and recorded. As shown in Fig. 3A, higher amounts of  $\text{H}_2\text{O}_2$  were detected with increasing concentrations of glucose in the presence of AuNPs, indicating that the AuNPs possessed high glucose oxidase-like activity. In addition, the higher the concentration of AuNPs and the longer the incubation time, the more  $\text{H}_2\text{O}_2$  was produced (Fig. 3B). Nanozymes made from different nanomaterials have been found to have several intrinsic enzyme-like properties, including peroxidase-like activity, oxidase-like activity, superoxide dismutase-like activity, protease-like activity, and so on<sup>22</sup>. Of note, one nanozyme may possess multiple catalytic activities compared to natural enzymes with specific catalytic activities. The enzymatic activities of AuNPs are highly dependent on the stabilizer used during the synthesis process<sup>23</sup>. For example, using BSA as the stabilizer endows AuNPs with both





glucose oxidase-like and peroxidase-like activity<sup>27</sup>. In our study, to construct self-supplied H<sub>2</sub>O<sub>2</sub> chemodynamic agents, a nanozyme with glucose oxidase-mimicking activity was the first requirement to produce intracellular H<sub>2</sub>O<sub>2</sub> via catalysis of glucose oxidation. Second, the selected nanozyme should not possess peroxidase-like activity to protect the produced H<sub>2</sub>O<sub>2</sub> from decomposition. Considering other aspects, including controllable, reproducible, and large-scale production, citrate-protected gold nanoparticles with glucose oxidase-like activity rather than peroxidase-like activity were chosen as the representative to investigate the anticancer efficiency of the Au@MPN<sup>27</sup>. Previous studies have reported that MPN can decompose in the presence of ATP

or in an acidic environment<sup>24,32,33</sup>. Therefore, we then explored the ATP- and pH-responsive disassembly behaviors of the Au@MPN by detecting the amount of released iron, which was quantified by using 1,10-phenanthroline. As shown in Fig. 3C, the release rate of iron increased as the pH value decreased. Under neutral or alkaline conditions, the phenolic hydroxyl groups of TA bind strongly to the metal ion through coordination interactions, while the acidic environment induces the protonation of the hydroxyl groups of TA, leading to weakening of the metal-polyphenol coordination<sup>34</sup>. In addition, iron release from the Au@MPN was observed in the presence of ATP, which was ascribed to the competitive binding of Fe(III) with ATP

through Fe-O-P coordination bonds<sup>24</sup> (Fig. 3D). Of note, the dual-responsive disassembly of MPN ensured the greatest utilization of metal ions compared to conventional metal-containing nanoparticles (e.g., Fe<sub>3</sub>O<sub>4</sub>)<sup>29,35,36</sup>. After the disassembly of MPN, the internal AuNPs were exposed to exert their glucose oxidase function and catalyze glucose oxidation to produce H<sub>2</sub>O<sub>2</sub>, which provided enough fuel for the Fenton reaction.

As Fe(II) has a higher catalytic performance in the Fenton reaction than Fe(III), we then investigated whether the released Fe(III) could be reduced by TA in an acidic environment. As shown in Fig. 3E and F, Fe(III) and TA formed an atropurpureus Fe-TA sediment at pH 7.0. In contrast, the Fe-TA sediment dissociated into Fe(III) and TA at pH 4.0, and some of the Fe(III) was reduced to Fe(II), forming orange complexes after reacting with phenanthroline. These results demonstrated that TA could convert Fe(III) to Fe(II) in an acidic environment, which could greatly improve the efficiency of chemodynamic therapy. To examine whether Au@MPN could produce H<sub>2</sub>O<sub>2</sub> in the presence of glucose for the subsequent Fenton reaction and generation of •OH, a methylene blue decolorization assay was conducted. Different concentrations of Au@MPN were mixed with 100 mM glucose and methylene blue at pH 4.0, and the absorbance at 664 nm was measured and recorded. As displayed in Fig. 3G, the Au@MPN could degrade methylene blue in a concentration-dependent manner in the presence of glucose in an acidic environment, which indicated that an efficient Fenton reaction occurred to produce •OH in this system. In contrast, Au@MPN could not degrade methylene blue in the absence of glucose, suggesting that Au@MPN without glucose could not provide H<sub>2</sub>O<sub>2</sub> for the Fenton reaction, thus leading to no •OH production (Fig. 3H). As expected, the addition of either glucose or H<sub>2</sub>O<sub>2</sub> could allow Au@MPN to generate •OH to degrade methylene blue. Of note, Au@MPN in the presence of both glucose and H<sub>2</sub>O<sub>2</sub> exhibited the most effective methylene blue degradation. Collectively, these results demonstrated that Au@MPN could be disassembled by ATP or low pH to release Fe(III), which was further reduced to Fe(II) to react with the self-supplied H<sub>2</sub>O<sub>2</sub> to efficiently generate •OH.

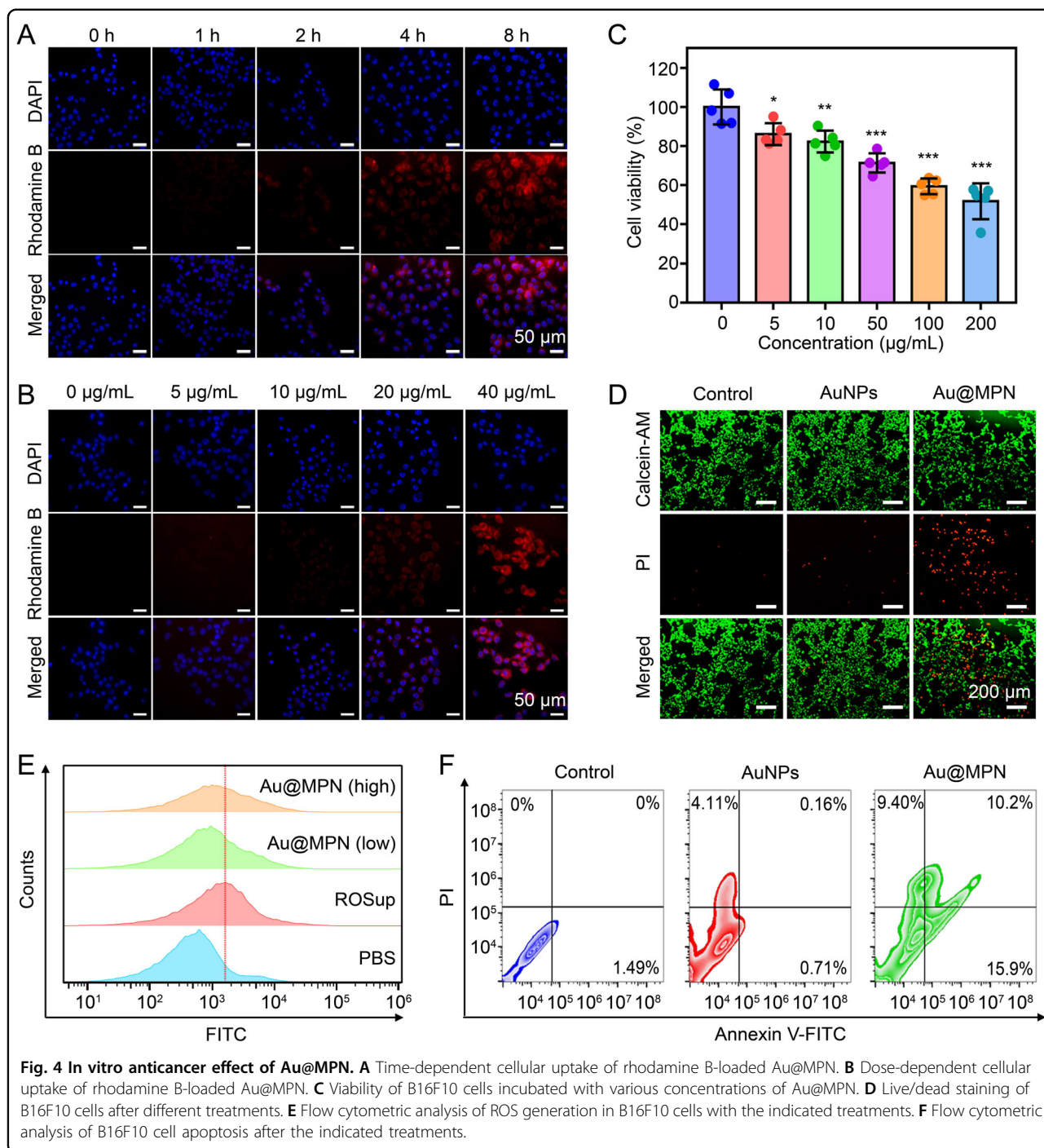
#### Anticancer effect of Au@MPN in vitro

As efficient cellular uptake was a prerequisite for good therapeutic effects, Au@MPN were labeled with rhodamine B to monitor intracellular uptake. As shown in Fig. 4A, red fluorescence was clearly observed in B16F10 cells with increasing incubation time. After 4 h, the cellular uptake of Au@MPN reached a plateau. In addition, the intracellular uptake of Au@MPN was dose-dependent, with obvious cellular uptake at a concentration of 40 µg/mL (Fig. 4B). These results were further confirmed by flow cytometry (Figs. S2 and S3). Next, cell viability after treatment with Au@MPN was examined by MTT assay.

As shown in Fig. 4C, the cell viability decreased as the concentration of Au@MPN increased. When the concentration of Au@MPN reached 200 µg/mL, the cell viability decreased to 51.8%. In the presence of H<sub>2</sub>O<sub>2</sub>, lower cell viability was observed after treatment with Au@MPN compared with the same concentration of Au@MPN in the absence of H<sub>2</sub>O<sub>2</sub> (Fig. S4). In addition, calcein-AM and PI double staining confirmed that Au@MPN could cause cell death (Fig. 4D). To decipher the underlying mechanism, cells treated with Au@MPN were stained with the dye DCFH-DA to evaluate the intracellular ROS level. The cells treated with PBS and ROSup were used as negative and positive controls. As expected, cells treated with both low and high Au@MPN concentrations exhibited a strong fluorescence signal, which indicated the generation of intracellular ROS (Fig. 4E and Fig. S5). Considering the high concentration of glucose in the medium (4.5 mg/mL), the Au@MPN could efficiently catalyze glucose to produce H<sub>2</sub>O<sub>2</sub>. Subsequently, TA reduced the released Fe(III) to generate highly catalytic Fe(II), which further reacted with H<sub>2</sub>O<sub>2</sub> in a highly efficient Fenton reaction. Furthermore, the annexin V-FITC and PI double staining method was employed to evaluate cell apoptosis. Consistent with the cell viability results, large numbers of cells (35.5%) treated with Au@MPN underwent apoptosis and necrosis compared to those in the control group (1.49%) and AuNPs group (4.98%). (Fig. 4F). Collectively, Au@MPN can effectively eradicate cancer cells due to the self-supplied H<sub>2</sub>O<sub>2</sub> and conversion of Fe(III) into Fe(II), thus resulting in the efficient and enhanced generation of •OH.

#### Antitumor effect of Au@MPN after intratumoral injection

Encouraged by the in vitro results, the antitumor effects of Au@MPN were further evaluated in vivo using B16F10-bearing mice as models. When the tumors reached 50 mm<sup>3</sup>, the mice were randomly divided into three groups and intratumorally injected with PBS, AuNPs, or Au@MPN (Fig. 5A). During the treatment period, the AuNPs showed little influence on tumor growth compared with PBS administration. In contrast, the mice injected with Au@MPN exhibited remarkable tumor growth inhibition (Fig. 5B–E). In addition, the photos and weights of the extracted tumors were in accordance with the results of the relative tumor volumes (Fig. 5F, G). Furthermore, H&E staining of tumor tissues showed damaged cell structures and scarce nuclei in the Au@MPN group, which indicated the effective antitumor activity of Au@MPN (Fig. 5H). Moreover, no obvious changes in body weight or histological abnormalities of the major organs were observed in the Au@MPN group, which suggested that intratumoral injection of Au@MPN induced no significant side effects in the mice (Fig. S6).



### Antitumor effect of Au@MPN after intravenous injection

Intratumoral injection has been applied to a limited selection of tumors, such as those present in liver or brain cancers. Therefore, investigation of intravenous administration is essential to expand the range of applications for treating various primary and metastatic tumors. The Au@MPN surface was coated with PEG (Au@MPN/PEG) to enhance colloidal stability in blood circulation. When the tumors reached 50 mm<sup>3</sup>, the mice were randomly

divided into three groups and intravenously injected with PBS, AuNPs, or Au@MPN/PEG (Fig. 6A). Compared with the PBS and AuNPs groups, the growth rate of the tumors of the mice treated with Au@MPN/PEG was considerably slower (Fig. 6B–E). Additionally, the tumors extracted from the mice in the Au@MPN/PEG group had the lowest weight compared with the PBS and AuNPs groups (Fig. 6F, G). Moreover, H&E staining was employed to investigate the pathological features of the tumors from

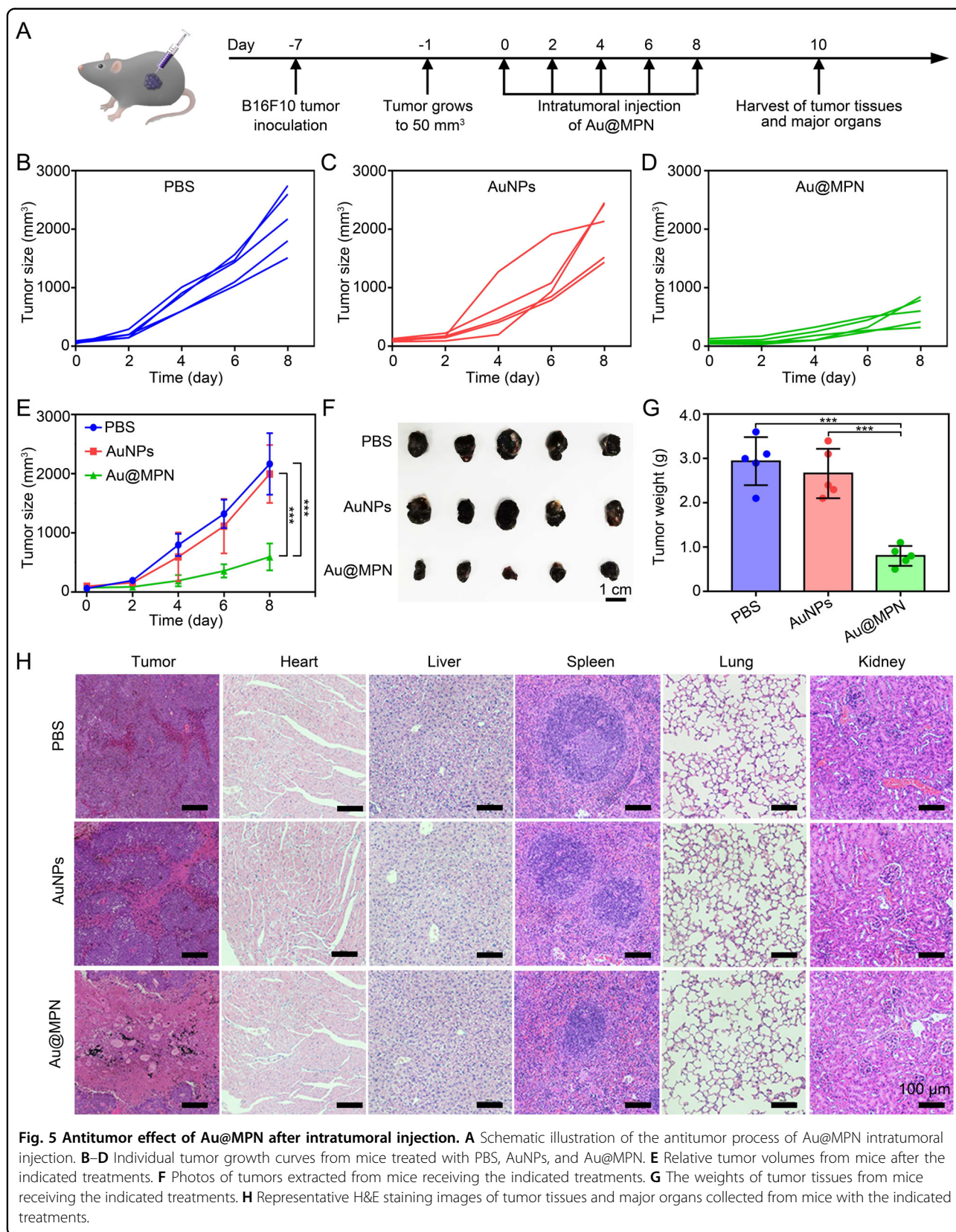


**Fig. 5** Antitumor effect of Au@MPN after intratumoral injection. **A** Schematic illustration of the antitumor process of Au@MPN intratumoral injection. **B–D** Individual tumor growth curves from mice treated with PBS, AuNPs, and Au@MPN. **E** Relative tumor volumes from mice after the indicated treatments. **F** Photos of tumors extracted from mice receiving the indicated treatments. **G** The weights of tumor tissues from mice receiving the indicated treatments. **H** Representative H&E staining images of tumor tissues and major organs collected from mice with the indicated treatments.

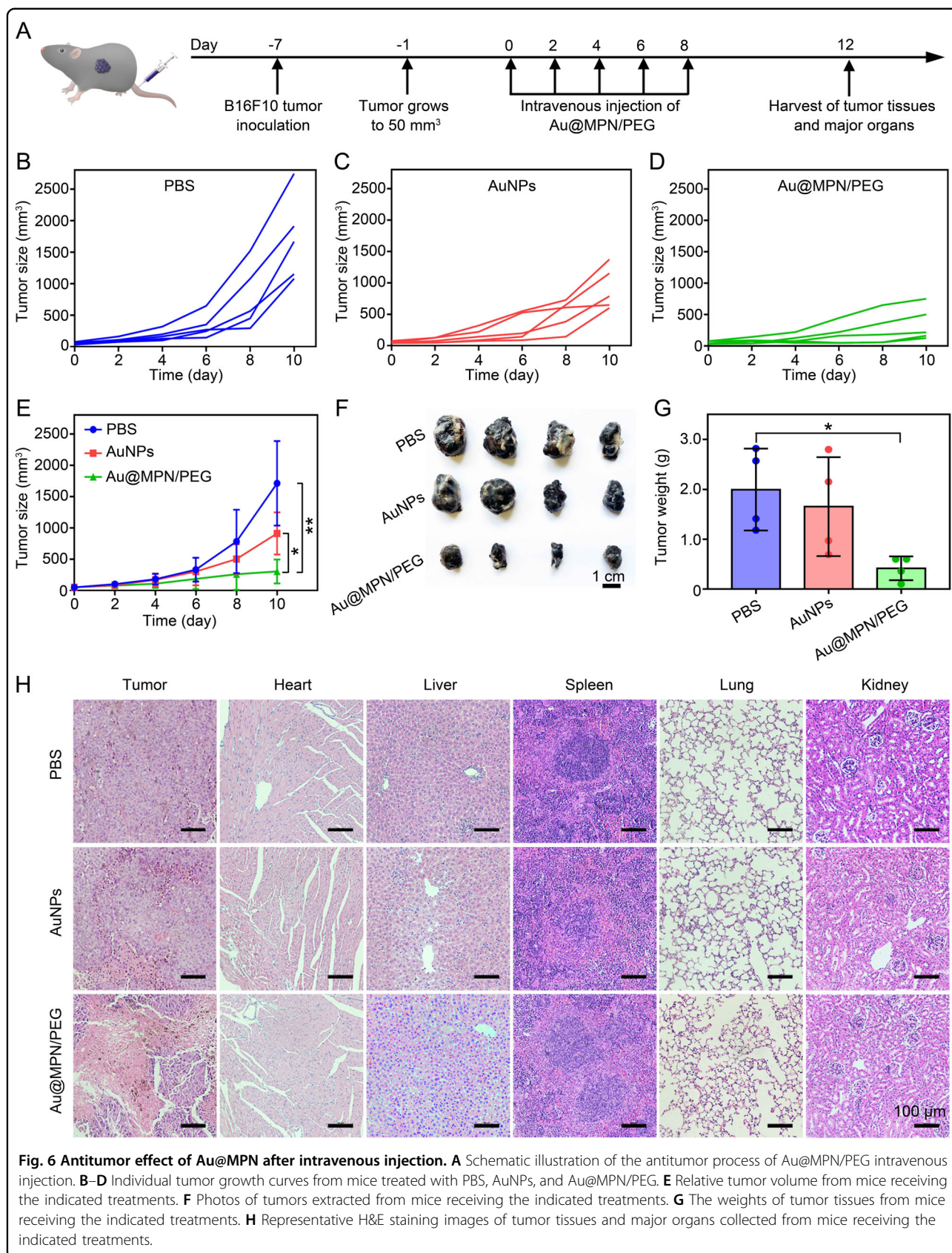
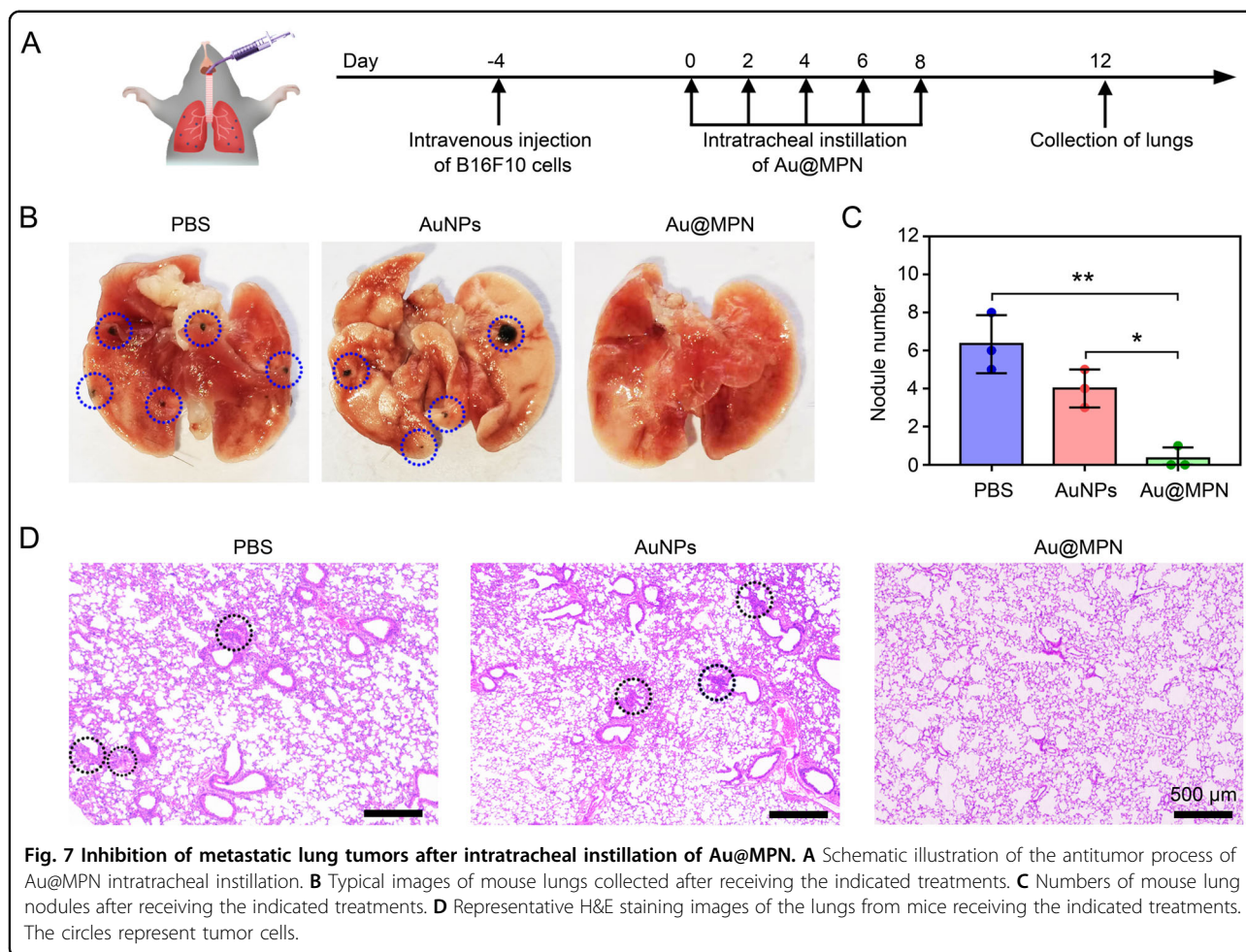


**Fig. 6 Antitumor effect of Au@MPN after intravenous injection.** **A** Schematic illustration of the antitumor process of Au@MPN/PEG intravenous injection. **B–D** Individual tumor growth curves from mice treated with PBS, AuNPs, and Au@MPN/PEG. **E** Relative tumor volume from mice receiving the indicated treatments. **F** Photos of tumors extracted from mice receiving the indicated treatments. **G** The weights of tumor tissues from mice receiving the indicated treatments. **H** Representative H&E staining images of tumor tissues and major organs collected from mice receiving the indicated treatments.



each group. As expected, histological analysis indicated extensive necrosis and tumor destruction in the Au@MPN/PEG group (Fig. 6H). Body weight and H&E staining of the major organs from the AuNP and Au@MPN/PEG groups showed no significant changes compared to the PBS group, thus demonstrating the good biocompatibility of the therapeutic process (Fig. S7). Collectively, tumor growth can be effectively suppressed by Au@MPN after both intratumoral and intravenous administration.

#### Inhibition of lung metastasis through intratracheal instillation of Au@MPN

Encouraged by the good therapeutic effect of Au@MPN to treat primary tumors, we further examined the inhibition of metastatic tumors using a B16F10 metastatic melanoma lung cancer mouse model. After 4 days of intravenous injection of B16F10 cells, mice were treated with PBS, AuNPs, and Au@MPN via intratracheal instillation, which allowed the solutions to distribute throughout the lungs in a physiological manner with high reproducibility, accuracy, and efficacy (Fig. 7A)<sup>37</sup>. As

shown in Fig. 7B and C, intratracheal instillation of Au@MPN significantly reduced the melanoma nodules relative to the PBS and AuNPs groups, which indicated superior suppression of lung metastasis. Additionally, the histological study revealed no obvious metastatic tumor cells in the lungs of mice treated with Au@MPN (Fig. 7D). In addition, no significant difference in body weight was found among these three groups (Fig. S8). Moreover, no obvious inflammation or lesions in the major organs were observed, which further confirmed the biocompatibility of Au@MPN (Fig. S9). Collectively, the dual-responsive disassembly of Au@MPN with the abilities to self-supply H<sub>2</sub>O<sub>2</sub> and carry out an autocatalytic Fenton reaction could effectively suppress the growth of primary tumors and metastatic melanoma lung tumors.

#### Conclusions

In summary, a core-shell nanoplatform with dual-responsive disassembly properties was constructed for enhanced chemodynamic therapy through its abilities to self-supply H<sub>2</sub>O<sub>2</sub> and carry out an autocatalytic Fenton reaction. We demonstrated that both ATP and low pH

could induce the disassembly of Au@MPN to release Fe(III), which was further reduced by TA into Fe(II) to act as a Fenton agent with high catalytic efficiency. In addition, the exposed AuNPs catalyzed the oxidation of glucose to generate H<sub>2</sub>O<sub>2</sub> in situ, which could react with Fe(II) to enhance the generation of •OH. Our results demonstrated that the Au@MPN had a good eradication effect against both primary tumors and metastatic melanoma lung tumors. Benefiting from the general adhesive property of polyphenols, this work may provide a universal strategy for constructing chemodynamic agents that can self-supply H<sub>2</sub>O<sub>2</sub> by replacing AuNPs with other nanozymes with glucose oxidase-like activity. Therefore, we anticipate that this work may open new avenues to conceive a strategy for improving the efficiency of tumor therapy.

#### Acknowledgements

This work was supported by the National Key Research and Development Program of China (2019YFA0111300), the National Natural Science Foundation of China (51903256, 21907113, 22277155, 52202359, 32001012, 22002190), the Science and Technology Program of Guangzhou (202102010225, 202102010217, 202102010284), the Guangdong Provincial Science and Technology Program (International Scientific Cooperation, 2018A050506035), the Guangdong Basic and Applied Basic Research Foundation (2022A1515012253, 2020A1515010305), the China Postdoctoral Science Foundation (2021M693674), and the Guangdong Provincial Pearl River Talents Program (2019QN01Y131).

#### Author details

<sup>1</sup>Laboratory of Biomaterials and Translational Medicine, Center for Nanomedicine, Department of Dermato-Venereology, The Third Affiliated Hospital, Sun Yat-sen University, 510630 Guangzhou, China. <sup>2</sup>School of Materials Science and Engineering, Peking University, 100871 Beijing, China. <sup>3</sup>Institutes of Life Sciences, School of Medicine, South China University of Technology, 510006 Guangzhou, China. <sup>4</sup>Guangdong Provincial Key Laboratory of Liver Disease Research, 510630 Guangzhou, China

#### Author contributions

M.P., E.J., and Y.X. contributed equally to this work. M.P.: conceptualization, methodology, investigation, validation, writing—original draft; E.J.: conceptualization, methodology, visualization, writing—review and editing, resources, funding acquisition, supervision; Y.X.: methodology, investigation, resources, funding acquisition; Y.W.: methodology, investigation, resources; S.L.: methodology, investigation, resources; D.S.: methodology, investigation, resources; H.W.: methodology, investigation, resources; Y.T.: conceptualization, methodology, writing—review and editing, visualization, resources, funding acquisition, supervision; Y.Z.: conceptualization, methodology, writing—review and editing, resources, supervision; and M.L.: conceptualization, methodology, writing—review and editing, visualization, resources, funding acquisition, supervision.

#### Conflict of interest

The authors declare no competing interests.

#### Publisher's note

Springer Nature remains neutral with regard to jurisdictional claims in published maps and institutional affiliations.

**Supplementary information** The online version contains supplementary material available at <https://doi.org/10.1038/s41427-022-00447-8>.

Received: 19 July 2022 Revised: 12 October 2022 Accepted: 25 October 2022.

Published online: 2 December 2022

#### References

- Esteve, A. et al. Dermatologist-level classification of skin cancer with deep neural networks. *Nature* **542**, 115–118 (2017).
- Schadendorf, D. et al. Melanoma. *Lancet* **392**, 971–984 (2018).
- Formenti, S. C. et al. Radiotherapy induces responses of lung cancer to CTLA-4 blockade. *Nat. Med.* **24**, 1845–1851 (2018).
- Haas, L. et al. Acquired resistance to anti-MAPK targeted therapy confers an immune-evasive tumor microenvironment and cross-resistance to immunotherapy in melanoma. *Nat. Cancer* **2**, 693–708 (2021).
- Sullivan, R. J. et al. Atezolizumab plus cobimetinib and vemurafenib in BRAF-mutated melanoma patients. *Nat. Med.* **25**, 929–935 (2019).
- Chen, Q. et al. In situ sprayed bioresponsive immunotherapeutic gel for post-surgical cancer treatment. *Nat. Nanotechnol.* **14**, 89–97 (2019).
- Li, H. et al. Disrupting tumour vasculature and recruitment of aPDL1-loaded platelets control tumour metastasis. *Nat. Commun.* **12**, 1–10 (2021).
- Zheng, C. et al. Engineering nano-therapeutics to boost adoptive cell therapy for cancer treatment. *Small Methods* **5**, 2001191 (2021).
- Jiang, W., Wang, Y., Wargo, J. A., Lang, F. F. & Kim, B. Considerations for designing preclinical cancer immune nanomedicine studies. *Nat. Nanotechnol.* **16**, 6–15 (2021).
- Tang, Z., Zhao, P., Wang, H., Liu, Y. & Bu, W. Biomedicine meets fenton chemistry. *Chem. Rev.* **121**, 1981–2019 (2021).
- He, H. et al. Cleavable bimetallic-organic polymers for ROS mediated cascaded cancer therapy under the guidance of MRI through tumor hypoxia relief strategy. *Sci. China Chem.* **63**, 936–945 (2020).
- Tang, Z., Liu, Y., He, M. & Bu, W. Chemodynamic therapy: tumour microenvironment-mediated fenton and fenton-like reactions. *Angew. Chem. Int. Ed.* **58**, 946–956 (2019).
- Liu, Z. et al. GSH-induced chemotaxis nanomotors for cancer treatment by ferroptosis strategy. *Sci. China Chem.* **65**, 989–1002 (2022).
- Ma, S. et al. A ROS-responsive aspirin polymeric prodrug for modulation of tumor microenvironment and cancer immunotherapy. *CCS Chem.* **2**, 390–400 (2020).
- Cao, R. et al. Protein nanoparticles containing Cu (II) and DOX for efficient chemodynamic therapy via self-generation of H<sub>2</sub>O<sub>2</sub>. *Chin. Chem. Lett.* **31**, 3127–3130 (2020).
- Dang, W. et al. 3D printed bioceramic scaffolds as a universal therapeutic platform for synergistic therapy of osteosarcoma. *ACS Appl. Mater. Inter.* **13**, 18488–18499 (2021).
- Liu, C. et al. An open source and reduce expenditure ROS generation strategy for chemodynamic/photodynamic synergistic therapy. *Nat. Commun.* **11**, 1–9 (2020).
- Gao, S. et al. Self-Supply of O<sub>2</sub> and H<sub>2</sub>O<sub>2</sub> by a nanocatalytic medicine to enhance combined chemo/chemodynamic therapy. *Adv. Sci.* **6**, 1902137 (2019).
- Lin, L.-S. et al. Synthesis of copper peroxide nanodots for H<sub>2</sub>O<sub>2</sub> self-supplying chemodynamic therapy. *J. Am. Chem. Soc.* **141**, 9937–9945 (2019).
- Fu, L.-H., Qi, C., Lin, J. & Huang, P. Catalytic chemistry of glucose oxidase in cancer diagnosis and treatment. *Chem. Soc. Rev.* **47**, 6454–6472 (2018).
- Fu, L. H., Qi, C., Hu, Y. R., Lin, J. & Huang, P. Glucose oxidase-instructed multimodal synergistic cancer therapy. *Adv. Mater.* **31**, 1808325 (2019).
- Wu, J. et al. Nanomaterials with enzyme-like characteristics (nanozymes): next-generation artificial enzymes (II). *Chem. Soc. Rev.* **48**, 1004–1076 (2019).
- Jiang, D. et al. Nanozyme: new horizons for responsive biomedical applications. *Chem. Soc. Rev.* **48**, 3683–3704 (2019).
- Zhang, L. et al. An adenosine triphosphate-responsive autocatalytic fenton nanoparticle for tumor ablation with self-supplied H<sub>2</sub>O<sub>2</sub> and acceleration of Fe (III)/Fe (II) conversion. *Nano Lett.* **18**, 7609–7618 (2018).
- Ding, Y. et al. A nanomedicine fabricated from gold nanoparticles-decorated metal-organic framework for cascade chemo/chemodynamic cancer therapy. *Adv. Sci.* **7**, 2001060 (2020).
- Zheng, C., Li, M. & Ding, J. Challenges and opportunities of nanomedicines in clinical translation. *BIO Integr.* **2**, 57–60 (2021).
- Zhang, H., Liang, X., Han, L. & Li, F. “Non-Naked” gold with glucose oxidase-like activity: a nanozyme for tandem catalysis. *Small* **14**, 1803256 (2018).
- Xu, J. et al. Ultrasmall gold nanoclusters-enabled fabrication of ultrafine gold aerogels as novel self-supported nanozymes. *Small* **18**, 2200525 (2022).
- Guo, Y., Sun, Q., Wu, F. G., Dai, Y. & Chen, X. Polyphenol-containing nanoparticles: synthesis, properties, and therapeutic delivery. *Adv. Mater.* **33**, 2007356 (2021).

30. Caruso, F., Spasova, M., Salgueiriño-Maceira, V. & Liz-Marzán, L. Multilayer assemblies of silica-encapsulated gold nanoparticles on decomposable colloid templates. *Adv. Mater.* **13**, 1090–1094 (2001).
31. Rahim, M. A. et al. Coordination-driven multistep assembly of metal-polyphenol films and capsules. *Chem. Mater.* **26**, 1645–1653 (2014).
32. Wang, Z. et al. Metal-phenolic-network-coated dendrimer-drug conjugates for tumor mr imaging and chemo/chemodynamic therapy via amplification of endoplasmic reticulum stress. *Adv. Mater.* **34**, 2107009 (2022).
33. Dai, Y. et al. Toxic reactive oxygen species enhanced synergistic combination therapy by self-assembled metal-phenolic network nanoparticles. *Adv. Mater.* **30**, 1704877 (2018).
34. Song, X.-R. et al. Polyphenol-inspired facile construction of smart assemblies for ATP- and pH-responsive tumor MR/optical imaging and photothermal therapy. *Small* **13**, 1603997 (2017).
35. Yan, J. et al. Engineering radiosensitizer-based metal-phenolic networks potentiate STING pathway activation for advanced radiotherapy. *Adv. Mater.* **34**, e2105783 (2022).
36. Zhang, Z. et al. Polyphenol-based nanomedicine evokes immune activation for combination. *Cancer Treat. Angew. Chem. Int. Ed.* **60**, 1967–1975 (2021).
37. Tian, X. et al. Pulmonary delivery of reactive oxygen species/glutathione-responsive paclitaxel dimeric nanoparticles improved therapeutic indices against metastatic lung cancer. *ACS Appl. Mater. Interfaces* **13**, 56858–56872 (2021).